Monolayer Junctions via Nanoparticles: A High-yield, Scalable Solution for Ambient-stable Molecular Devices

Gabriel Puebla-Hellmann[1,2*], Koushik Venkatesan[3], Marcel Mayor[2], and Emanuel Lörtscher[1]

[1] IBM Research - Zurich, Säumerstrasse 4, CH-8803 Rüschlikon, Switzerland
[2] Department of Chemistry, University of Basel, St. Johanns-Ring 19, CH-4056 Basel, Switzerland
[3] Department of Chemistry, University of Zurich, Winterthurerstrasse 190, CH-8057 Zürich, Switzerland

***Abstract*—Electrically contacting monolayers of molecules enables devices that can exploit their intrinsic functionality for novel applications ranging from electronics based on quantum properties to tailored photonics and analyte-selective sensors. Various electrical molecular functionalities have been demonstrated, for example diodes [1], negative differential resistors [2], switches [3], electroluminescence [4] and molecular sensing [5]. These proof-of-concept experiments, however, were mainly performed with single-molecule junctions created by mechanical manipulation, which are not mass-fabrication compatible. By using a self-assembled monolayer (SAM) rather than single-molecule junctions, the intrinsic functionality of the molecular building blocks can be exploited without requiring sub-atomic control over the junction geometry. Nevertheless, it has not yet been possible to fabricate SAM-based devices without compromising film integrity, functionality or mass-fabrication compatibility. Here, we present a generic process based on a layer of metallic nanoparticles deposited onto the SAM in a conformal and non-destructive fashion, which simultaneously addresses all mentioned issues enabling high-yield mass-fabrication of ambient-stable devices. Statistical analysis of several thousand devices shows that the nanoparticle layer allows the fabrication of metal–molecule–metal junctions with active areas ranging in size from several thousand $\mu\mathrm{m}^2$ down to thousands of nm^2, with high device-to-device reproducibility and without metal-filament formation. Systematic variation of the SAM composition further demonstrates that the intrinsic molecular properties are not affected by the nanoparticle layer or the subsequent top metallization. The concept is generic to mono- and multilayers and opens an avenue for the integration of molecular building blocks into a solid-state, wafer-scale architecture that is scalable down to the single-molecule entity.**

Keywords: Molecular Electronics, SAM, Transport, Integration, Nanoparticles

Using intrinsic molecular functionality is an attractive concept in terms of novel devices. Single-molecule junctions, however, suffer from a direct dependence of their behavior on the exact junction configuration, and the sub-atomic accuracy required for reproducibility cannot be achieved with current fabrication techniques. In contrast, the metal–SAM–metal architecture constrains the junction configurations and creates an ensemble average, potentially mitigating device-to-device variations. Furthermore, a layer-by-layer approach in which self-assembly provides the sub-atomic resolution in the junction direction allows such devices to be fabricated with conventional methods.

The crucial aspect in a SAM-based approach is the top-contact formation. This step should maintain film integrity as well as intrinsic functionality, while being mass-fabrication compatible and scalable in terms of active area. Various strategies have been proposed, ranging from direct evaporation onto cooled films in nanopores [6] over PEDOT:PSS [7] and graphene [8] contact layers to EGaIn liquid-metal top electrodes [9], micro-contact printing [10], and metal-transfer methods [11]. Each strategy has drawbacks, for example, low yield due to metal-filament penetration of the SAM [12], [13] or high series resistance [14], that prevent any of those strategies from concurrently fulfilling the above-mentioned requirements.

To address all these issues, we use metallic nanoparticles deposited from solution onto the SAM to provide a metallic, conformal and protective layer. The device geometry, schematically shown in Fig. 1 **a**, is based on a platinum bottom electrode, onto which the molecular monolayer is assembled (Fig. 2 **b**). A dielectric matrix constrains the molecules laterally into circular pores of variable diameter, from 70 μm down to 60 nm. Nanoparticles are deposited onto the molecular layer from solution (Fig. 1 **c**), and the top contact is subsequently reinforced by direct metal evaporation (Fig. 1 **d**), sealing the device.

Platinum is chosen as the bottom-contact material because it is compatible with complementary metal-oxide semiconductor (CMOS) fabrication. This choice does not affect the quality of the SAMs [15], and the contact resistance of sulfur anchors to Pt is even lower than the one to commonly used gold [16]. We use conventional physical vapor deposition to avoid exotic fabrication methods. This results in a roughness of 0.4 nm RMS over 1 $\mu\mathrm{m}^2$, which can be further improved by a factor of 2 using wafer-scale template stripping [17].

The prototypical SAM consists of alkane-thiol molecules compromising an alkane backbone with n carbon units and one (monothiol) or two (dithiol) anchor groups. As alkanes rapidly form robust and well-ordered monolayers, they have been implemented in most SAM-based platforms and are useful for comparison. We use alkane-dithiols here, as the nanoparticle layer needs a top anchor group to adhere to. The second anchor group, however, introduces additional phases, such as the lying-down or the looped phase [18], and can result in multi-layer formation. Appropriate assembly conditions can suppress these issues [19], [18], [20]. We study backbones with 4 to 10 carbon units, rather than 8 to 16 as used typically. These shorter backbones allow an accurate assessment of the top-contact series resistance and the protective quality of the

nanoparticles, albeit, at the cost of a lower film quality [21]. Nanoparticles are deposited onto the SAM from solution to form an initial metallic top-contact layer in a non-destructive and conformal manner [22]. A non-polar solvent is required to enable contact between the liquid interface and the SAM [23]. Agglomeration of nanoparticles in the solvent is suppressed by weakly bound ligands, which can be displaced locally to allow the formation of a chemical bond between the nanoparticle and the top anchor group of the molecules. This thiol bond immobilizes the particles and creates an electrical metal–molecule contact. The use of spherical particles reduces the area of molecules in contact with the top electrode: for 3-nm particles by a factor of approximately 100, which can be optimized further by using smaller particles that are cubic in shape.

Comparing atomic force microscopy scans (Fig. 1 **e**) of an empty pore (dashed black curve) and of a pore with the SAM ($\approx$ 2 nm thickness) and nanoparticles (3 nm diameter) assembled (solid blue curve), we find an average depth difference between the two scans of roughly 5 nm. The nanoparticles form a continuous film on the SAM, with the thickness varying between one and two monolayers, but do not deposit on the dielectric. A metal layer is subsequently added via physical vapour deposition, creating electrical contact to and among the particles while hermetically sealing the pore (Fig. 1 **d**). An optical image of part of a chip is shown in Fig. 1 **f**, with the inset showing a single pore. In this work, gold nanoparticles are used because of the wide availability of mono-disperse solutions, but they can readily be replaced by platinum or palladium particles for CMOS-material compatibility. Here, fabrication is performed on 100-mm wafers up to the film assembly. In principle, however, the full process can be up-scaled to larger wafer dimensions.

The individual molecular devices are characterized by their current-voltage (I–V) characteristics, obtained with triangle bias sweeps, starting at 0 V and ranging to 1.0 V and -1.0 V, respectively. Individual chips accommodate 62 arrays with 61 different pore diameters each, of which at least 54 arrays per chip are characterized. A maximum of 3782 devices and a logarithmic scaling of the active area enable a statistical evaluation.

In the following, we will initially discuss data from devices incorporating 1,10 decane-dithiols. An I–V density plot combining the raw data of the three different pore diameters 790 nm, 1.8 μm and 5.5 μm is shown in Fig. 2 **a** (no filtering or averaging). The figure combines three density plots, with each color (yellow, orange, blue) corresponding to the data obtained for one pore size (overlap is colored gray). We observe three distinct bundles with little overlap and a variation of less than half on order of magnitude, which demonstrates the reproducibility and low fluctuations of our approach. Variable temperature measurements are shown in Fig. 2 **b** for one device from each bundle. Upon cooling to 78 K, the current changes only slightly ($<$ 20 %), consistent with measurements performed on similar metal–molecule–metal devices [24]. We therefore conclude that nonresonant electron tunneling is maintained as the underlying transport mechanism through the alkane-dithiol monolayer [24].

Next, we focus on the relationship between the current I and the active area A. A density plot of the current at a bias of 0.2 V versus the active area is shown in Fig. 2 **c**. Each column represents data from 55 devices with nominally identical pore diameter. Histograms at diameters of 0.1, 1.0 , 9.8 and 53 μm are shown in Fig. 2 **d**. Low scatter, negligible outliers, and a linear dependence between I and A are visible, with A ranging from 4.1×10^9 nm^2 down to 5×10^3 nm^2 (the gap visible around 10^9 nm^2 is the result of an area range not covered in the design). We attribute the increased scatter for $A < 3 \times 10^5$ nm^2 to variations in the active area caused by imperfect etching of the dielectric.

Individual I–V curves can be categorized into three classes: open, linear and nonlinear. Fig. 2 **e** shows a graph of this class distribution as a function of A. An open fraction exceeding 10% is only observed for the two smallest pore diameters, which again indicates imperfect etching. For $A > 10^5$ nm^2, however, curves are only classified as linear or nonlinear. Over the entire range of A, 3204 devices (95.5%) are classified as nonlinear, 67 as open (2%) and 84 as linear (2.5%), proving that the nanoparticle layer successfully inhibits the formation of SAM-penetrating metal-filaments even for large A.

Beside a high device yield, reproducible device-to-device transport properties are mandatory for an application-oriented molecular platform. Fig. 2 **f** shows a density plot of the calculated current density, J, versus voltage, V, for the 3204 devices classified as nonlinear. A narrow distribution with a full width at half maximum of approximately 0.5 A/cm^2 is visible, the result of both ensemble averaging and a reduction in possible contact geometries. Furthermore, the devices are stable up to at least $\pm$1.0 V in bias, do not require any conditioning, and retain their transport properties for several months even when stored at ambient conditions (see SI).

The data presented demonstrates nonlinear responses with high yield and high device-to-device reproducibility. However, these characteristics could, in principle, have another origin than transport through the SAM. To confirm the molecular origin of the device response, we performed inelastic electron tunneling spectroscopy (IETS) and studied the dependence of transport on the alkane length: IETS spectra of two devices acquired at 4.2 K are shown in Fig. 3 **a**. The pore diameters are 7.6 and 8.5 μm, respectively. Various vibrational peaks are present, consistent with previous studies [25], [26]. A number of peaks present in both traces corresponds to characteristic molecular vibrations, namely, $\nu(\mathrm{C-S})$ (92 meV), $\delta_\mathrm{r}(\mathrm{CH_2})$ (115 meV), $\nu(\mathrm{C-C})$ (135 meV), $\gamma_{\mathrm{w,t}}\mathrm{CH_2}$, and $\delta_\mathrm{s}(\mathrm{CH_2})$ (185 meV). This inelastic electron-scattering signal provides evidence that transport is dominated by the SAM (further studies are necessary to identify all of the peaks observed).

Additional evidence of the molecular origin of the transport properties is provided by comparing devices with different alkane lengths of 4, 6, 8 and 10 carbon units (labeled C4, C6, C8 and C10, respectively), which also demonstrates the platform's flexibility in terms of compound dimensions. Fig.

3 **b** compares the mean and standard deviation of J, obtained for each compound by fitting a Gaussian to the histogram at each bias point. The curves are similar in functional behavior, with a shift in J and a decreased deviation for C10. An example histogram extracted at 0.5 V bias and reproduced in Fig. 3 **c**, shows four distinct and Gaussian-like distributions. In a simple model, the SAM is considered a tunnel barrier with $J \propto 10^{\beta d/2.303}$, where β is the decay coefficient and d the barrier width [27]. Extracting β from our data yields $\beta_n = (1.0 \pm 0.2)$ per carbon (Fig. 3 **d**), in agreement with literature values for through-bond tunneling [21], [12], [28]. This length dependence shows not only that the molecular layer maintains its physical and chemical integrity, but also that the SAM dominates the transport characteristics and is not masked by the contact resistance, and that Coloumb blockade effects [29] can be ruled out.

The molecular integration approach presented offers a simple and non-destructive top-contact formation step that yields metal–molecule–metal devices and is flexible in terms of molecular dimensions. Automated characterization of several thousand devices enables rapid screening of molecular building blocks, allowing an accelerated development of tailored electric functionality. Furthermore, the approach is not limited to electronic tasks, but can be augmented by optical and fluidic access to enable a variety of novel device concepts, with applications ranging from electrical switching over light emission and detection to ionic and molecular sensing.

Acknowledgment

The authors acknowledge technical support by M. Tschudy, U. Drechsler, and M. Buerge, as well as strategic support by B. Michel, W. Riess, and A. Curioni. Funding by the NCCR MSE and SNF NRP 62 is highly appreciated.

Author Information

Author Contributions

G.P.H. conceived, developed, and performed device fabrication, performed data collection and analysis, and wrote the manuscript. K.V. and M.M. provided chemical support and commented on the manuscript. E.M.L. initiated and supervised the project, contributed to the experimental setups and data analysis and wrote the manuscript.

Competing financial interests

The authors declare no competing financial interests.

Corresponding authors

Correspondence to:
G. Puebla-Hellmann (gpu@zurich.ibm.com)

References

[1] Elbing, M. *et al.* A single-molecule diode. *Proc. Nat. Acad. Sci. USA* **102**, 8815–8820 (2005).

[2] Chen, J., Reed, M. A., Rawlett, A. M. & Tour, J. M. Large on-off ratios and negative differential resistance in a molecular electronic device. *Science* **286**, 1550–1552 (1999).

[3] Schwarz, F. *et al.* Field-induced conductance switching by charge-state alternation in organometallic single-molecule junctions. *Nat. Nanotechnol.* **11**, 170–176 (2016).

[4] Marquardt, C. W. *et al.* Electroluminescence from a single nanotube-molecule-nanotube junction. *Nat. Nanotechnol.* **5**, 863–867 (2010).

[5] Ponce, J. *et al.* Effect of metal complexation on the conductance of single-molecular wires measured at room temperature. *J. Am. Chem. Soc.* **136**, 8314–8322 (2014).

[6] Zhou, C., Deshpande, M. R., Reed, M. A., Jones, L. & Tour, J. M. Nanoscale metal/self-assembled monolayer/metal heterostructures. *Appl. Phys. Lett.* **71**, 611–613 (1997).

[7] Akkerman, H. B., Blom, P. W. M., de Leeuw, D. M. & de Boer, B. Towards molecular electronics with large-area molecular junctions. *Nature* **441**, 69–72 (2006).

[8] Wang, G., Kim, Y., Choe, M., Kim, T.-W. & Lee, T. A new approach for molecular electronic junctions with a multilayer graphene electrode. *Adv. Mater.* **23**, 755–760 (2011).

[9] Nijhuis, C. A., Reus, W. F., Barber, J. R., Dickey, M. D. & Whitesides, G. M. Charge transport and rectification in arrays of SAM-based tunneling junctions. *Nano Lett.* **10**, 3611–3619 (2010).

[10] Loo, Y.-L., Lang, D. V., Rogers, J. A. & Hsu, J. W. P. Electrical contacts to molecular layers by nanotransfer printing. *Nano Lett.* **3**, 913–917 (2003).

[11] Jeong, H. *et al.* A new approach for high-yield metal-molecule-metal junctions by direct metal transfer method. *Nanotechnology* **26**, 025601 (2015).

[12] Lee, T. *et al.* Comparison of electronic transport characterization methods for alkanethiol self-assembled monolayers. *J. Phys. Chem. B* **108**, 8742–8750 (2004).

[13] Kim, T.-W., Wang, G., Lee, H. & Lee, T. Statistical analysis of electronic properties of alkanethiols in metal-molecule-metal junctions. *Nanotechnology* **18**, 315204 (2007).

[14] Neuhausen, A. B., Hosseini, A., Sulpizio, J. A., Chidsey, C. E. D. & Goldhaber-Gordon, D. Molecular junctions of self-assembled monolayers with conducting polymer contacts. *ACS Nano* **6**, 9920–9931 (2012).

[15] Lee, S. *et al.* Self-assembled monolayers on Pt(111): Molecular packing structure and strain effects observed by scanning tunneling microscopy. *J. Am. Chem. Soc.* **128**, 5745–5750 (2006).

[16] Beebe, J. M., Engelkes, V. B., Miller, L. L. & Frisbie, C. D. Contact resistance in metal-molecule-metal junctions based on aliphatic SAMs: Effects of surface linker and metal work function. *J. Am. Chem. Soc.* **124**, 11268–11269 (2002).

[17] Puebla-Hellmann, G., Mayor, M. & Lörtscher, E. Ultraflat nanopores for wafer-scale molecular-electronic applications. In *2015 IEEE 15th I. Conf. on Nanotechnology (IEEE-NANO)*, 1197–1201 (2015).

[18] Akkerman, H. B. *et al.* Self-assembled-monolayer formation of long alkanedithiols in molecular junctions. *Small* **4**, 100–104 (2008).

[19] Jia, J. *et al.* Lying-down to standing-up transitions in self assembly of butanedithiol monolayers on gold and substitutional assembly by octanethiols. *J. Phys. Chem. C* **117**, 4625–4631 (2013).

[20] Chah, S., Fendler, J. H. & Yi, J. In-situ analysis of stepwise self-assembled 1,6-hexanedithiol multilayers by surface plasmon resonance measurements. *Chem. Commun.* 2094–2095 (2002).

[21] Engelkes, V. B., Beebe, J. M. & Frisbie, C. D. Length-dependent transport in molecular junctions based on SAMs of alkanethiols and alkanedithiols: Effect of metal work function and applied bias on tunneling efficiency and contact resistance. *J. Am. Chem. Soc.* **126**, 14287–14296 (2004).

[22] Puebla-Hellmann, G., Lörtscher, E. & Mayor, M. Method to contact self-assembled monolayers of molecules (patent pending) YOR820152256 (2016).

[23] Sur, U. K. & Lakshminarayanan, V. Existence of a hydrophobic gap at the alkanethiol SAM-water interface: An interfacial capacitance study. *J. Colloid Interface Sci.* **254**, 410–413 (2002).

[24] Wang, W., Lee, T. & Reed, M. A. Mechanism of electron conduction in self-assembled alkanethiol monolayer devices. *Phys. Rev. B* **68**, 035416 (2003).

[25] Wang, W., Lee, T., Kretzschmar, I. & Reed, M. A. Inelastic electron tunneling spectroscopy of an alkanedithiol self-assembled monolayer. *Nano Lett.* **4**, 643–646 (2004).

[26] Jeong, H. *et al.* Investigation of inelastic electron tunneling spectra of metal-molecule-metal junctions fabricated using direct metal transfer method. *Appl. Phys. Lett.* **106**, 063110 (2015).

[27] Simmons, J. G. Low-voltage current-voltage relationship of tunnel junctions. *J. Appl. Phys.* **34**, 238–239 (1963).

[28] Simeone, F. C. *et al.* Defining the value of injection current and effective electrical contact area for EGaIn-based molecular tunneling junctions. *J. Am. Chem. Soc.* **135**, 18131–18144 (2013).
[29] Morita, T. & Lindsay, S. Determination of single molecule conductances of alkanedithiols by conducting-atomic force microscopy with large gold nanoparticles. *J. Am. Chem. Soc.* **129**, 7262–7263 (2007).
[30] Akkerman, H. B. *Large-area Molecular Junctions*. Ph.D. thesis, University of Groningen (2008).

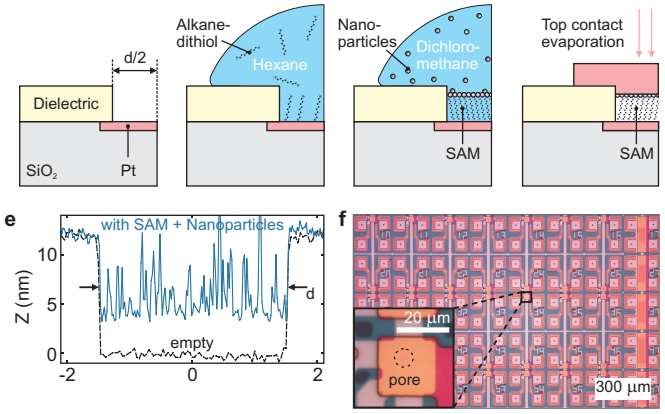

Fig. 1. **Device Fabrication. a,** Pores are etched into a dielectric film on a platinum electrode. **b,** Assembly of the SAM selectively on the electrode. **c,** Solution-based deposition of nanoparticles onto the SAM. **d**, Top contact evaporation. **e** Atomic force microscopy scans of an empty pore (black, dashed) and of a pore with SAM and nanoparticles (blue, solid) assembled therein. **f,** Optical image of device arrays. The inset shows a single device with the location of a micrometer-size pore indicated by the circle.

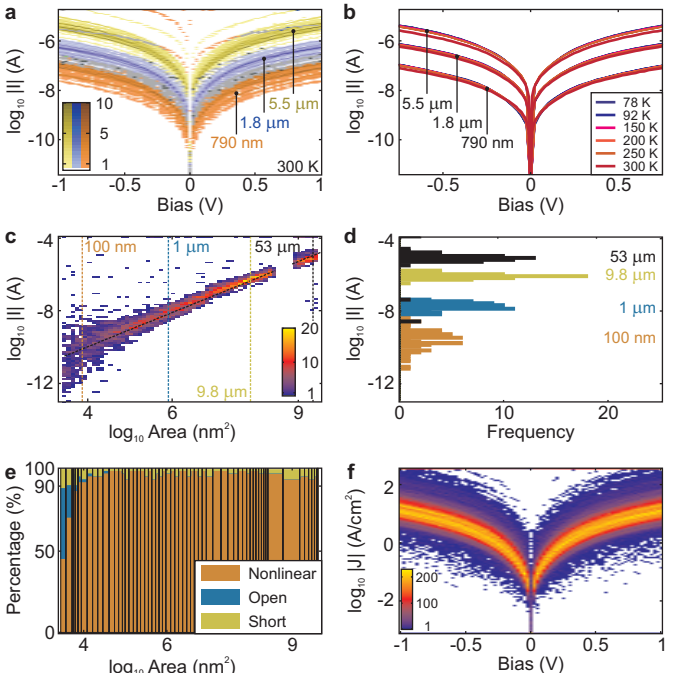

Fig. 2. **Transport properties of Pt–1,10 decane-dithiol–Au junctions. a,** I-V density plot for 3 pore diameters (790 nm, 1.8 um and 5.5 μm), comprising 55 devices each. **b,** Temperature-dependent I–V curves of one individual device for each pore diameter. **c,** I–A density plot over all pore sizes with 55 devices per size, extracted at a bias of 0.2 V. **d,** I histograms at four selected areas, A. **e,** Categorization of device characteristics versus A. **f,** J–V density plot of all 3204 nonlinear devices.

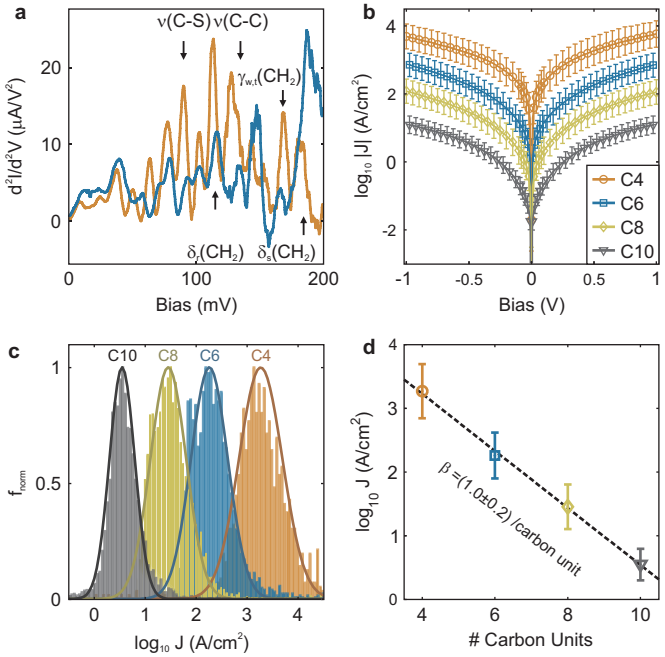

Fig. 3. **Molecular origin of the transport properties. a,** IETS spectra of 1,10 decanedithiol devices at 4 K, displaying molecular vibrational peaks. **b,** Mean current density, J, for C4, C6, C8 and C10 alkanedithiols. **c,** Histograms extracted at 0.5 V bias and corresponding Gaussian fits. **d,** Average J at 0.5 V bias versus backbone chain length and corresponding fit of the tunneling coefficient β.

I. Methods

A. Device Fabrication

Device fabrication is based on standard 4" silicon wafers with a 150–200-nm thick thermal oxide layer. Bottom electrodes consisting of 60 nm Pt with a 0.5-nm Ti adhesion layer are defined on the wafer via optical photolithography, electron-beam evaporation (Evatec BAK501LL) and lift-off. To deposit the dielectric, a two-step approach is used: first, an adhesion layer of titanium oxide (4 cycles) and a layer of silicon nitride (50 cycles, $\approx$ 3 nm) are deposited via Atomic Layer Deposition (Oxford ALD), yielding a low-quality protective layer. Second, Plasma Enhanced Physical Vapour Deposition (PECVD) is used to deposit 10 nm of high-quality silicon nitride (Oxford PECVD).

Pores are etched in the dielectric using two methods: first, large features are defined via photolithography and etched using buffered hydrofluoric acid (BHF). Second, micron and sub-micron features are patterned via electron-beam lithography and a combination of reactive-ion etching (Oxford NPG 80, CHF_3/O_2) and wet etching (BHF). The wafers are then cleaned in piranha etch (3:1 H_2SO_4:H_2O_2) and cleaved using a silicon scribe. Individual chips are plasma-cleaned (120 s Ar/H plasma, 900 s O plasma, TePla 100-E) before being immersed in solutions of the different molecular species. Dedicated glassware is used for the molecular solutions and plasma-cleaned before use. Molecular solutions are 50 mMol (C4/C6: 20 μl, C8/C10: 30 μ l in 3 ml hexane), freshly prepared using commercially available alkane-dithiols (Sigma Aldrich (C4,C6,C8), Alfa Aesar (C10)) and hexane (Sigma Aldrich) stored under argon. The glassware is then back-filled with argon, sealed and stored in a light-shielded box for 2-3 h (C4, C6) or 20-24 h (C8, C10). After rinsing twice with hexane and drying with nitrogen, the chips are placed in a 0.1 g/L solution of nanoparticles (3-nm, PVP, NanoPartz) in dichloromethane (Sigma Aldrich) for 90 s and then dried with nitrogen.

The 20 nm thick gold top electrode is deposited via electron-beam evaporation, with a rate ramping from 0 to 0.2 nm/s over approximately 20 s. The electrode is then patterned via photolithography using a standard resist (MicroChemicals AZ6612), omitting any baking steps, and ion milling (Oxford Ion Fab). Chips are then oxygen-plasma-cleaned (PVA TePla Gigabatch, 200 W, 120 s) and rinsed in acetone/isopropanol to remove the resist.

B. Data Acquisition and Processing

Devices were characterized at room temperature and ambient conditions using an automated probe station (Cascade Summit 12000) combined with a semiconductor parameter analyzer (HP B1500A). Temperature-dependent measurements were performed in vacuum in a liquid-nitrogen-cooled probe station (Janis). The temperature was controlled using a controller (Lakeshore) and a heating element. For IETS measurements, samples were bonded to a chip carrier, mounted in a home-made dip stick and immersed in liquid helium. The DC and AC (337.3 Hz, 4 mV RMS) components of the signal, generated by a lock-in amplifier (Stanford Instruments, SR830), were combined and low-pass (1 kHz) filtered via an adder/filter (Stanford Instruments, SR560) and applied to the sample. The second harmonic signal was detected by the same lock-in amplifier.

All I-V data is presented as measured without any post-processing. The current density J is calculated using the active area as determined by SEM imaging. IETS measurements have been smoothed using 5-point boxcar averaging.

For automatic curve characterization, the following definitions are used: curves with an average current below 25 pA are classified as open, curves whose resistance at 300 mV is within 10% of that at 50 mV are classified as linear and all other curves are categorized as nonlinear. Example curves are provided in the SI.

II. Supplementary Information

A. Bottom Electrode Characterization

The electrode's surface morphology is a significant factor influencing the assembly of the SAM and hence the properties of the entire device. In particular, deposition and etching of the dielectric film on top of the electrode should not degrade the electrode surface. The surface roughness is investigated using atomic force microscopy (Veeco Dim V, Tapping Mode with Nanosensors Pointprobe+ tips). An EBL/RIE-defined pore is shown in Fig. 4 **a**, the small particles visible on the dielectric areas around the pore are likely remaining resist. A smaller scan of the exposed electrode surface is shown in Fig. 4 **b**, where a roughness of 0.39 nm RMS over 1 μm^2 is extracted, similar to the roughness of the electrode prior to deposition and etching.

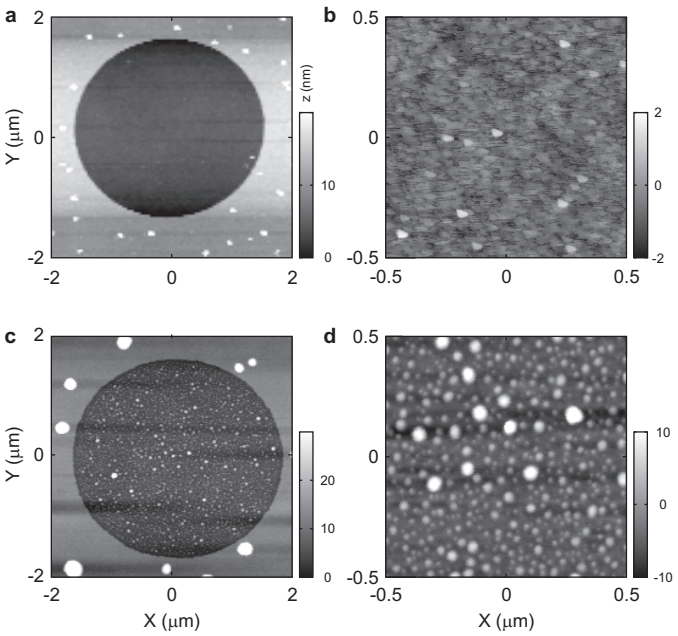

Fig. 4. **a** Atomic force microscopy scan of a 2.7 μm diameter pore. **b** The surface at the bottom of the pore with a roughness of 0.39 nm RMS. **c** A similar pore after film growth and nanoparticle deposition. **d** Scan of the surface inside the pore, showing circular particles.

B. Nanoparticle Film Characterization

After deposition of the molecular monolayer and the nanoparticles, a similar pore was scanned, shown in Fig. 4 **c**. The inside of the pore is significantly roughened and the pore has a reduced depth. A smaller scan of the surface inside the pore is shown in Fig. 4 **d** and shows round features not present before, as expected for a nanoparticle layer. We observe an increase in roughness from 0.39 nm RMS to 3.18 nm RMS over 1 μm^2. As the lateral resolution is limited by convolution of the topology with the tip radius (7-10 nm radius), the film surface is difficult to image. We observe round structures of different dimensions, up to 10-15 nm height and 40-50 nm apparent diameter. While the dispersion of the utilized nanoparticles is stated to be 20 %, these protrusions may both be gold, ligand agglomerates or both. In both cases, such features reduce the effective area and an optimization of the nanoparticle dispersion and deposition process will be required.

C. High Resolution Transmission Electron Microscopy of a Finished Device

To investigate the interface between the nanoparticle film and top electrode, Transmission Electron Microscopy (TEM) was performed on a cross-section of a measured C10 device. A TEM lamella was extracted from the device using a focused gallium ion beam system. After extraction, the lamella was thinned down to a width of approximately 40 nm and loaded into a TEM system, where images where taken at 200 kV acceleration voltage. An overview image is shown in Fig. 5 **a**, where the SAM separates the top and bottom electrode (bright layers) on the left side. The slightly thicker separation on the right side is the SiNx dielectric. The top electrode is mainly flat but shows warped regions, one of which is shown at higher magnification in Fig. 5 **b**. Here, the SAM region separating top and bottom electrode is clearly visible. We also observe small voids in the top electrode which may have their origin in the larger protrusions visible in the AFM scans. More importantly, we observe no apparent features reminiscent of nanoparticles, suggesting that the particles have fused with the top electrode.

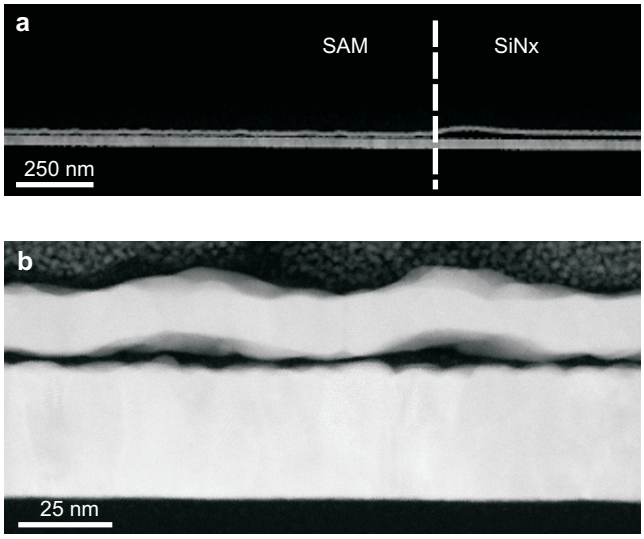

Fig. 5. **a** Cross-section TEM images of part of a C10 device. Both the Pt bottom and Gold top electrode are visible as bright layers, separated by the SAM on the left side and the SiNx dielectric on the right. The top electrode is warped in some regions. **b** Zoom into a warped region: the bottom electrode, SAM region and top electrode are clearly visible, as well as the electron deposited platinum protection layer for extraction of the lamella (grainy area at the top of the image).

Increasing the magnification yields close to atomic resolution, as visible in Fig. 6 **a** and **b**, where the crystal lattices and grain boundaries of both electrodes become visible. However, no features on the size scale of 3 nm are visible, which

implies that the ligands have been displaced and the particles have fused to create a uniform, albeit rough, top electrode. Note that due to the low scattering coefficient of carbon, the alkanedithiol SAM is not visible in these images.

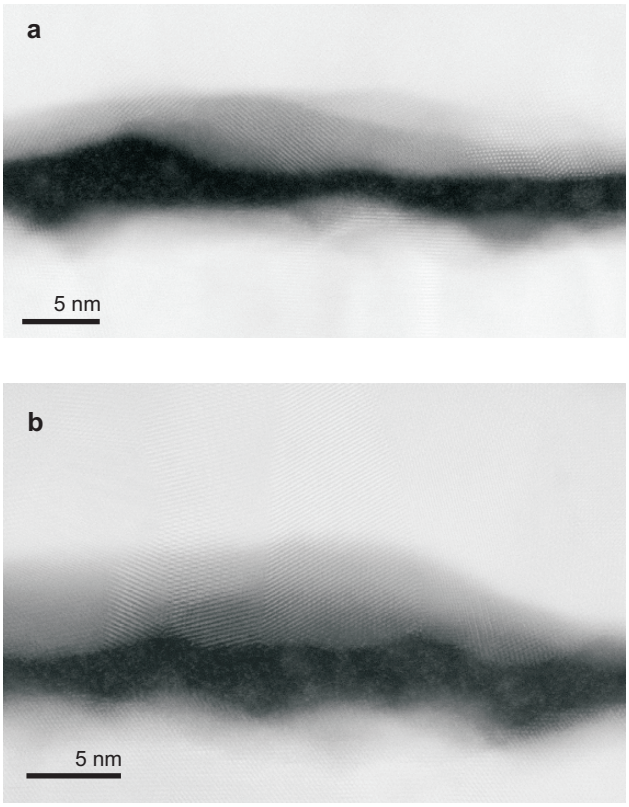

Fig. 6. **a** and **b**: High resolution TEM images of the SAM region. While crystal lattices are visible, no 3 nm sized features can be identified which would correspond to nanoparticles.

To ensure, that the top electrode close to the SAM is indeed gold, we perform energy dispersive X-ray spectroscopy on the top electrode, in close ($\approx$ 2 nm) vicinity of the SAM. The resulting spectrum is shown in Fig. 7, peaks where automatically identified by the software. Three elements are detected: carbon, gold and copper. The carbon and copper peaks are always present due to background carbon in the chamber and copper from the sample holder. We therefore conclude that the top electrode consists mainly of gold and carbon and the particles visible in the AFM images are indeed either gold or carbon.

D. I–V Characterization

For datasets with several thousand I–V curves, an automated routine is required to differentiate between different types of device behavior. We differentiate between three types: open, linear and non-linear. The categorization algorithm works as follows: first, all curves with an average absolute current below 25 pA are categorized as open, three examples are shown in Fig. 8 **a**. The cut-off value is above our noise floor

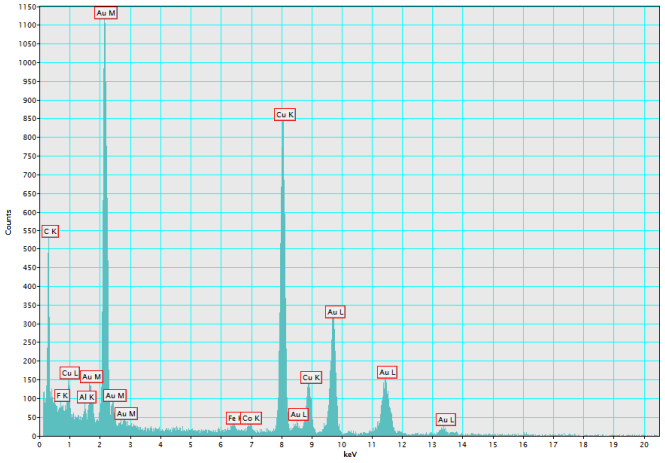

Fig. 7. Energy dispersive X-ray spectrum of a region located $\approx$ 2 nm above the SAM. Three elements yield a signal: carbon, gold and copper.

($\approx$ 10 pA) and also removes samples with low signal-to-noise (blue curve), where the differentiating between linear and non-linear is difficult. For the remaining curves, the algorithm calculates the deviation δ between the resistances at 50 mV and 300 mV: $\delta = |1 - R_{50\mathrm{mV}}/R_{300\ \mathrm{mV}}|$. Curves with a $\delta < 0.1$ are categorized as linear, the others as non-linear. Sample curves for different δ are shown in Fig. 8 **b**, where the top two are categorized as linear, the bottom two as non-linear. Note that the current is normalized for a better comparison. The two bias values are chosen such that the lower point still yields good signal-to-noise for small pores and the upper value such that shorted curves are not in current compliance, which would lead to a false categorization as non-linear. The cut-off value of 0.1 is chosen such that a smaller non-linearity, for example due to joule heating of a short, is still categorized as linear.

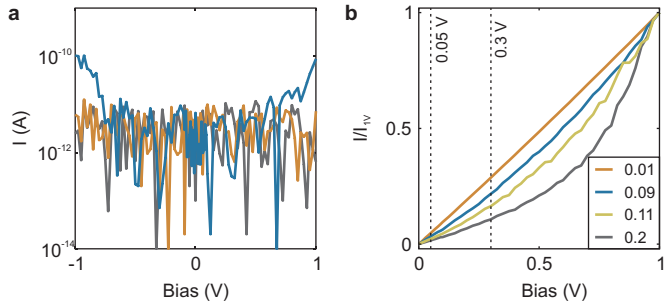

Fig. 8. **a** Three example curves classified as open. **b** Four example curves with different ratios of resistance at 50 mV and 300 mV bias. The top two are categorized as linear, while the lower two are categorized as non-linear.

E. Temperature Dependence

Transport through molecules can be the result of a number of different mechanisms such as, for example, resonant or off-resonant tunneling, hopping or thermionic emission [24]. The temperature dependence of the transport properties can

help distinguish between these mechanisms. In case of alkane-dithiols, the conduction mechanism is expected to be off-resonant tunneling [**?**] which, for low bias, can be described by the Simmons model and is expected to be temperature independent [27]. As alkane-thiol SAMs are often implemented in large-area molecular junctions, literature is available on the temperature dependent transport properties of these devices. For metal-molecule-metal junctions, no significant temperature was found for three different manufacturing approaches: nanopores[24], direct evaporation on larger pores[13] and direct metal transfer [11]. Similar results where obtained for PEDOT devices[7], with the notable exception of Neuhausen *et al*, which attributed the dependence to the different polymer used[14].

To demonstrate the weak temperature dependence in our devices, Fig. 9 shows Arrhenius plots for two of the three devices shown in Fig. 1 **b**, the third is omitted for clarity. Both devices show a slight temperature dependence with a tendency to higher current at lower temperature for higher bias, similar to the trend observed by Jeong *et al*[11], and consistent in magnitude with other work[24], [13], [7].

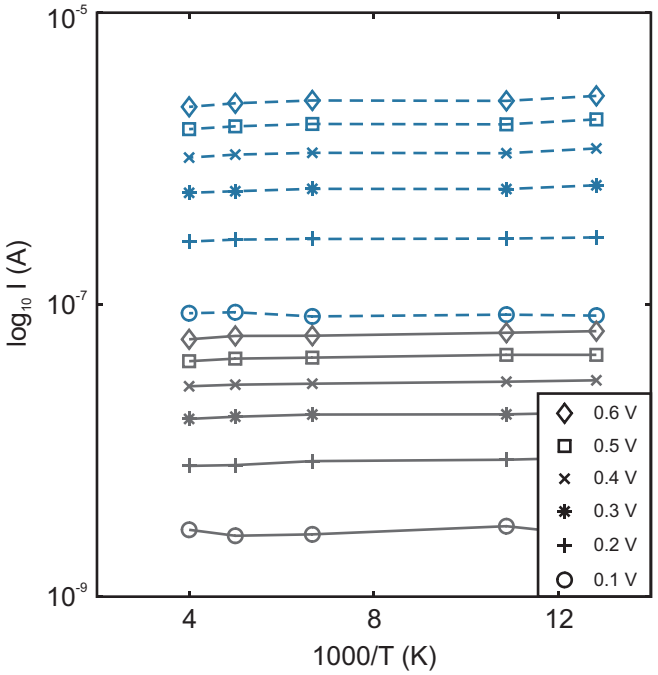

Fig. 9. Arrhenius plot for two devices (790 nm diameter: solid blue, 5.5 μm: dashed black), showing a very slight temperature dependence.

F. Additional Information for Devices Based on C4, C6 and C8

In general, we observe similar behavior for all four species of molecules investigated. However, the film quality decreases for decreasing chain length, which leads to an increased number of defects, larger scatter and lower stability of the final devices. Histograms of the current I versus active area A at a bias of 0.2 V as well as of the current density J versus bias are shown in Fig. 10 and Fig. 11 respectively. We obtain excellent results for C6, C8 and C10, with typically 80% or more nonlinear behaviour, as shown in Fig. 12. For the shortest chain length, two slopes are visible in the I-A histogram, as linear curves are not excluded from the data shown, which also broadens the peaks in the J-V histogram. While the yield is significantly reduced (Fig. 12 **a**), such short molecules are often not investigated at all. Here, we demonstrate that the approach presented can be also be used for films of typically low quality.

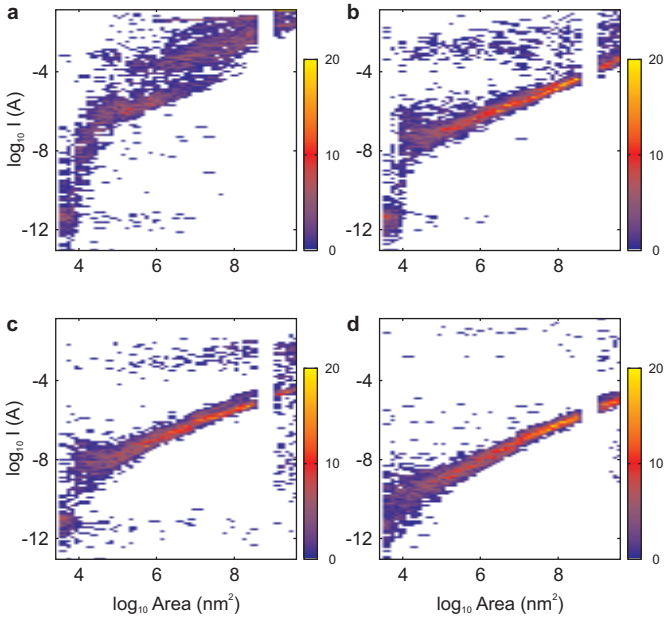

Fig. 10. **Histogram of I vs A: a,** C4, **b,** C6, **c,** C8 and **d,** C10.

G. Device Repeatability and Stability

In addition to the comparison between devices, single device stability and repeatability are also desirable. One aspect is the stability of the I–V curves obtained, as SAM-based molecular electronic devices often require a number of voltage sweeps for their properties to stabilize. Because each device is characterized by a triangle sweep, we can compare the upward and downward sweeps to characterize the single-sweep repeatability. A histogram of the current ratio between upward and downward sweeps at a bias of 0.5 V bias obtained for C10 devices is shown in Fig. 13 **a**. Out of a total of 3355 devices, 3171 are classified as nonlinear on both sweeps, compared with 3204 on the upward sweep. The data presented only incorporates the devices classified as nonlinear on both sweeps. As visible from the graph, 58% (1867/3171) of the devices exhibit a current difference of less than 0.5%. Furthermore, 93% (2949/3171) are within 10%, demonstrating excellent sweep stability.

A second aspect is long-term stability, for which a part of the C10 chip was measured a second time after storage

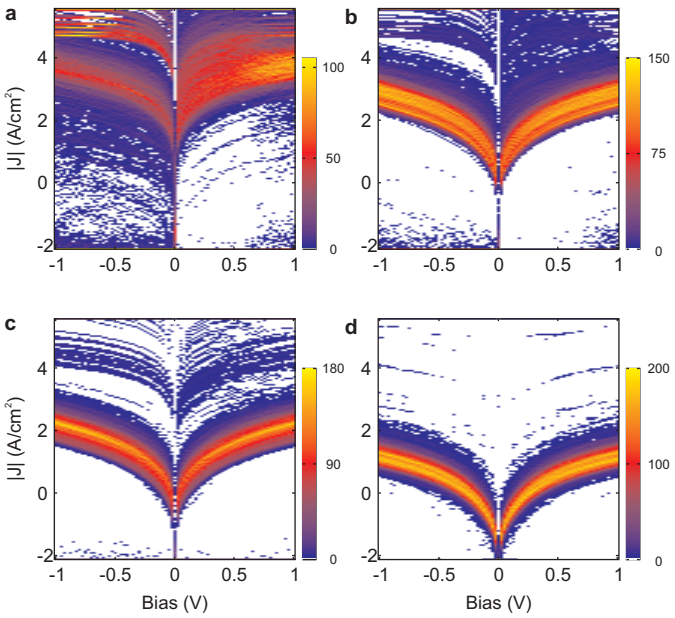

Fig. 11. **Histogram of J vs V: a,** C4, **b,** C6, **c,** C8 and **d,** C10. The full datasets are shown, including shorts and opens.

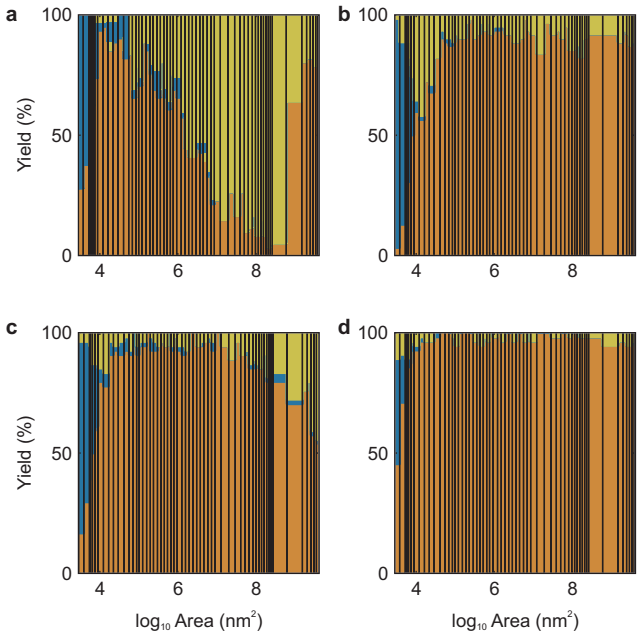

Fig. 12. **I-V curve categorization: a,** C4, **b,** C6, **c,** C8 and **d,** C10.

at ambient conditions for 136 days. In contrast to PEDOT devices, which only recover their initial properties in vacuum [30], the data presented is obtained under ambient conditions without further treatment. The ratio of the initial current to the current measured after 136 days is shown as a histogram in Fig. 13 **b**. A distinct peak is visible at a ratio of one, indicating stable devices, and a second peak is visible close to 0.75. Half

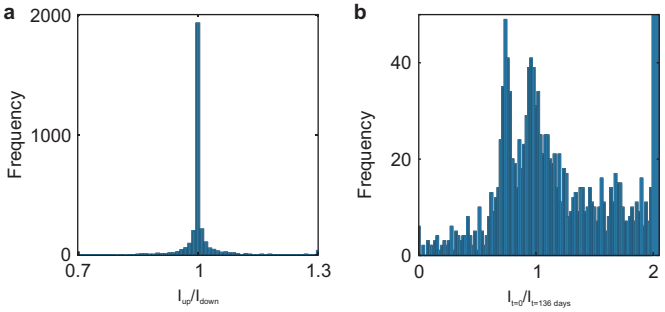

Fig. 13. **Stability a** Histogram of the current ratio between upward and downward sweep at 0.5 V. **b** Histogram of the current ratio between the initial sweep and the sweep taken 136 days later, at 0.5 V.

of the devices are in the interval between 0.6 and 1.4, even though the devices have been cycled several times between 77 K and 300 K. The second peak mainly originates from pores with an area exceeding 1000 μm^2 and although the reason for this consistent behavior is currently unclear it may relate to the very large active area and therefore increased amount of defects in the SAM. As the top electrode in the current devices is comparatively thin (20 nm), we expect better stability in future devices with a thicker top layer.